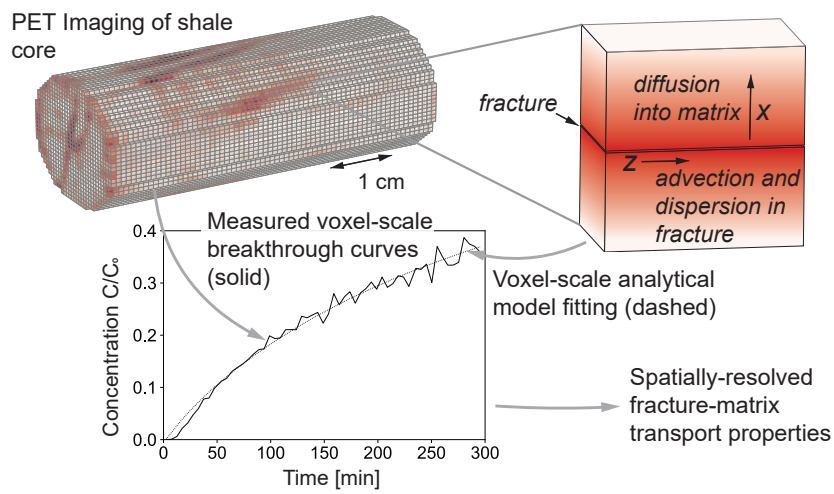


1 Graphical Abstract

2 **Quantification of the impact of acidified brine on fracture-matrix**
3 **transport in a naturally fractured shale using in situ imaging and**
4 **modeling**

5 Christopher Zahasky, Manju Pharkavi Murugesu, Takeshi Kurotori, Collin Sut-
6 ton, Jennifer L. Druhan, Bolivia Vega, Sally M. Benson, Anthony R. Kavscek



7 Quantification of the impact of acidified brine on
8 fracture-matrix transport in a naturally fractured shale
9 using in situ imaging and modeling

10 Christopher Zahasky^{a,*}, Manju Pharkavi Murugesu^b, Takeshi Kurotori^b,
11 Collin Sutton^a, Jennifer L. Druhan^c, Bolivia Vega^b, Sally M. Benson^b,
12 Anthony R. Kavscek^b

^a*Department of Geoscience University of Wisconsin-Madison Madison WI 53706 United States*

^b*Department of Energy Science & Engineering Stanford University Stanford CA 94305 United States*

^c*Department of Geology University of Illinois at Urbana-Champaign Urbana IL 61801 United States*

13 **Abstract**

Understanding flow, transport, chemical reactions, and hydro-mechanical processes in fractured geologic materials is key for optimizing a range of subsurface processes including carbon dioxide and hydrogen storage, unconventional energy resource extraction, and geothermal energy recovery. Flow and transport processes in naturally fractured shale rocks have been challenging to characterize due to experimental complexity and the multiscale nature of quantifying continuum scale descriptions of mass exchange between micrometer-scale fractures and nanometer-scale pores. In this study, we use positron emission tomography (PET) to image the transport of a conservative tracer in a naturally fractured Wolfcamp shale core before and after exposure of the core to low pH brine conditions. Image-based experimental observations are interpreted by fitting an analytical transport model to fracture-containing voxels in the core. Results of this analysis indicate subtle increases in matrix diffusivity and a slightly more uniform fracture velocity distribution following exposure to low pH conditions. These observations are compared with a multi-component one-dimensional reactive transport model that indicates the capacity for a 10% increase in porosity at the fracture-matrix interface as a result of the low pH brine exposure. This

*Corresponding author email: czahasky@wisc.edu

porosity change is the result of the dissolution of carbonate minerals in the shale matrix to low pH conditions. This image-based workflow represents a new approach for quantifying spatially-resolved fracture-matrix transport processes and provides a foundation for future work to better understand the role of coupled transport, reaction, and mechanical processes in naturally fractured rocks.

14 *Keywords:* shale, fractures, X-ray computed tomography, positron emission
15 tomography, reactive transport, models

16 **1. Introduction**

17 A quantitative and predictive understanding of transport across fracture-
18 matrix interfaces in shale formations is vital to the management and engineering
19 of a range of flow and transport processes. These processes include groundwater
20 protection from infiltrating contaminants [1], storage security of geologically
21 sequestered CO₂ [2, 3, 4], resource recovery following hydraulic fracturing [5, 6,
22 7], and long-term nuclear waste storage security [8, 9].

23 Flow and transport processes between fractures and matrix/host rock mate-
24 rial have been quantitatively described with a range of numerical and analytical
25 modeling approaches. Large fracture networks have been modeled with mul-
26 tiple interacting continua approaches (e.g. dual porosity, dual permeability)
27 [10, 11, 12, 13, 14], or large discrete fracture networks where the fractures are
28 explicitly defined [15, 16]. Simulation of flow in a small number of fractures can
29 be accomplished using explicit flow field modeling by solving the Navier-Stokes
30 equation when fracture geometry can be constrained or approximated [17, 18],
31 or using hybrid or micro-continuum approaches [19, 20].

32 In addition to numerical approaches, analytical models have been derived to
33 describe solute and reactive transport in fractured systems [21, 22]. Describing
34 solute transport into matrix material with analytical models often relies on the
35 assumption that the matrix can be considered infinite and the concentration
36 of solute in the fracture is constant [21, 23]. A more sophisticated solution

37 was derived to account for advection and dispersion in the fracture [24]. Semi-
38 analytical solutions have been expanded to solve for these processes in two
39 dimensions along a single fracture [25]. The advantage of these analytical meth-
40 ods is that they can be readily applied to solve for transport parameters within
41 simple systems or sub-domains (i.e. voxels) within more complex systems.

42 A key barrier to predictive understanding of transport between fracture and
43 matrix in many geologic settings is quantifying flow and transport processes
44 in response to changing fluid chemistry conditions. In many contexts, the
45 overprinting of natural environmental conditions by anthropogenic activities
46 results in transient variations in pore fluid chemistry that can drive precipi-
47 tation and dissolution reactions that alter fracture-matrix transport behavior
48 [26, 27, 28, 20]. The mineralogical composition of shale rocks is often catego-
49 rized into the proportion of shale matrix composed of carbonate minerals (e.g.
50 calcite and dolomite), silicates (e.g. quartz, feldspars, and pyrite), and clays
51 (e.g. illite and smectite) [6] and these differences in composition have been
52 observed to influence local matrix transport properties [29]. In the presence of
53 complex brines, and when subject to rapid shifts in pH and solute chemistry, this
54 multi-component and multispecies system presents a highly coupled, non-linear
55 reactive transport problem [30] requiring numerical reactive transport models
56 to track and predict behavior [31, 32, 33, 34, 35, 30, 36, 37].

57 Multiscale quantification of flow, transport, and reactions is often compli-
58 cated by uncertainty about the applicability of experimental batch measure-
59 ments under ambient conditions to larger-scale dynamic system behavior [38].
60 In cases where flow-through experiments are performed under elevated pressure
61 and temperature, typically only bulk measurements of transport properties are
62 possible [39]. X-ray computed tomography (X-ray CT) is a key tool that has
63 been extensively used to recover three-dimensional information about fracture
64 geometry and fracture evolution under in situ conditions in geologic materials
65 [40, 41, 42, 43, 44, 27, 4]. However, while X-ray CT is ideal for geometric quan-
66 tification, measurement of solute transport is challenging with X-ray CT due to
67 the need to use high photon attenuating tracers [45]. These tracers can create

68 gravitational artifacts and have very low signal-to-noise ratios as solute concen-
69 tration decreases. These challenges are amplified in samples with micron-scale
70 fracture apertures [46, 45, 47, 48].

71 Positron emission tomography (PET) is a complementary in situ imaging
72 technique that relies on the detection of high-energy photons produced from in-
73 jected positron-emitting radiotracers. Tomographic reconstruction methods are
74 then used to acquire three-dimensional time-lapse images of radiolabeled com-
75 pound distributions in geologic materials. This three-dimensional imaging pro-
76 vides thousands of concentration measurements as a function of time throughout
77 a sample, enabling multiscale transport quantification. The 511 keV photons
78 emitted during positron emission and annihilation events are ideally suited for
79 geologic materials that otherwise cause significant photoelectric adsorption and
80 attenuation of lower energy photons [45]. This technique has recently been used
81 to quantify solute advection and dispersion in highly heterogeneous sandstones
82 under saturated and unsaturated flow [49, 50, 51] and to quantify absorption in
83 microporous carbonates [52].

84 In this study, we employ PET imaging to provide the unprecedented quan-
85 tification of spatially variable fracture-matrix transport associated with natural
86 fractures in a Wolfcamp formation shale sample before and after acidic reactive
87 fluid injection. Slug radiotracer injection with simultaneous PET imaging is per-
88 formed and an analytical solution to the advection-dispersion equation is used to
89 interpret voxel-scale fracture-matrix transport. A weak acidified brine injection
90 (pH=4) was then performed for 21 days followed by a repeated slug tracer imag-
91 ing experiment. This second post-acid experiment enabled the quantification of
92 changes in transport behavior resulting from extended exposure to low pH con-
93 ditions. A multi-component numerical reactive transport model (RTM) is con-
94 structed to confirm the extent of reactive alteration based on acid-neutralizing
95 solubilization of carbonate minerals at the fracture-matrix interface. The RTM
96 offers independent verification of the interpretation of experimentally-observed
97 changes in fracture-matrix transport behavior.

98 **2. Methods**

99 *2.1. Sample characterization and brine fluid chemistry*

100 The core used in this study is a cylindrical Wolfcamp shale core with a
101 diameter of 25 mm and a length of 58 mm acquired from the Permian Basin at
102 a depth of 2867 m. Mineral composition and organic content of the core were
103 measured using X-ray diffraction analysis and source rock analysis, respectively.
104 Both measurements were conducted by Core Laboratories. Core mineralogy and
105 organic characteristics are shown in Table A.3 and were reported in previous
106 studies [53]. Synthetic brine was created following the Wolfcamp brine recipe
107 (Table 1) that was previously developed to establish chemical equilibrium with
108 Wolfcamp shale, thus minimizing reactivity prior to the acidification experiment
109 [37].

Table 1: Composition of synthetic brine solution.

Composition	Potassium Chloride	Calcium Chloride	Magnesium Chloride	Sodium Chloride	Sodium Nitrate	Sodium Sulphate	Sodium Bicarbonate
wt%	1.1	5.23	1.49	90.9	0.06	0.80	0.39

110 *2.2. Experimental CT data acquisition*

111 The Wolfcamp core sample was first dried for 120 hours in a vacuum oven
112 at 45°C until the sample mass stabilized. The core was sealed between the
113 coreholder inlet and outlet end caps using high-strength heat-shrink fluorinated
114 ethylene propylene tubing. The core was then wrapped with an aluminum foil
115 to provide a gas diffusion barrier [54, 50]. The coreholder inlet and outlet end
116 caps had flow channels connecting to the core with dead volumes of 0.58 cm³
117 and 0.98 cm³, respectively. The core was placed into a high-pressure aluminum
118 sleeve that enabled the application of confining pressure using tap water as the
119 confining fluid. The seal around the core was pressure-tested for 24 hours to
120 ensure complete isolation of pore fluids from the confining fluid.

121 Prior to pore fluid injection, a confining pressure of 1720 kPa (250 psi) was
122 applied and the sample was vacuumed using a vacuum pump (*Leybold D16B*,
123 ultimate pressure: 1×10^{-4} mbar). With the vacuum applied, the sample was
124 imaged daily using an X-ray CT scanner (*GE LightSpeed*) operated at 140 kV
125 and 120 mA with an exposure of 1 second per scan. The raw voxel size was
126 $195 \times 195 \times 625 \mu\text{m}^3$ and the field of view of was 10 cm. Complete vacuum was
127 reached when the CT number in Hounsfield units of the core ceased to decrease
128 further. These X-ray CT scans provide dry baseline scans for subsequent poros-
129 ity and fluid saturation measurements and monitoring [41].

130 The core was then saturated with krypton gas (99.999% purity) at 2068 kPa
131 (300 psi) and confining pressure of 3790 kPa (550 psi). Krypton is an inert gas
132 with a large X-ray attenuation coefficient relative to other gases [55]. The higher
133 X-ray attenuation coefficient increases the contrast between the baseline scan
134 and the krypton-saturated scan. This provides a more accurate quantification
135 of the 3D porosity distribution in the core, which is calculated via linear scaling
136 [41, 53].

137 The core was then vacuumed again and saturated with CO_2 (100% purity)
138 at 2068 kPa (300 psi) before injecting the prepared synthetic brine solution
139 described in Table 1. The core is saturated with CO_2 prior to brine injection
140 because of the higher solubility of CO_2 relative to air. This ensures that any
141 gas that is not displaced during brine injection will be dissolved in the brine
142 and transported out of the core [53]. To initially saturate the core, the brine
143 was injected at a pressure of 3650 kPa (530 psi) with a backpressure of 3170
144 kPa (460 psi) and confining pressure of 4826 kPa (700 psi). Pyrite oxidation
145 was minimized by purging nitrogen gas through the injected brine used in all
146 experiments to displace any dissolved oxygen. All pressure conditions were
147 controlled by high-pressure syringe pumps (*Teledyne ISCO*) as schematically
148 illustrated in Figure 1. The brine imbibition process was monitored and the
149 core was determined to be fully saturated based on X-ray CT scans [53].

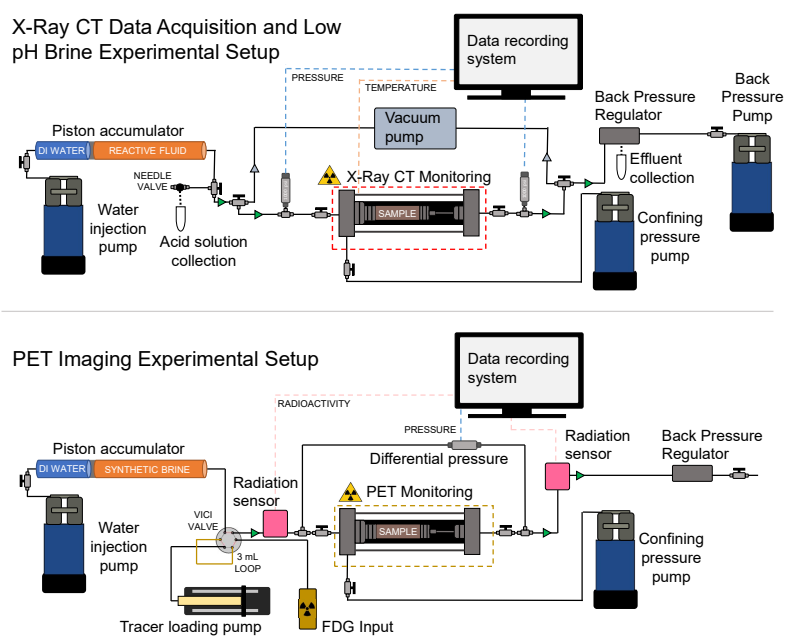


Figure 1: Schematic illustrations of the experimental setups for reaction (top) and PET imaging experiments (bottom).

150 *2.3. Experimental positron emission tomography data acquisition*

151 Two sets of tracer experiments imaged with PET were performed, one before
152 the low-pH brine injection and one after the low-pH brine injection as described
153 in the following section. PET imaging experiments were performed with an ex-
154 perimental platform schematically described in the lower illustration of Figure
155 1. This platform is specifically designed for the safe injection, quantification,
156 and disposal of radiotracers with simultaneous in situ PET imaging. Continu-
157 ous aqueous phase injection was achieved with a *Vindum VP-3K* dual piston
158 pump plumbed to a 1000 mL *Parker* piston accumulator filled with the brine
159 mixture described in Table 1. The fluid injection rate for both PET imaging
160 experiments was 0.01 mL/min. The pore pressure conditions at this flow rate
161 were approximately 2000 kPa (290 psi), with the post-reaction pore pressure
162 being slightly higher due to the reduction of sample permeability resulting from
163 low pH brine exposure. A second *Vindum VP-6K* dual piston pump applied a
164 confining pressure to the core of 3790 kPa (550 psi). This confining pressure
165 was used in all PET imaging and low-pH brine injection procedures.

166 The positron-emitting radiotracer [^{18}F]-fluorodeoxyglucose (FDG) was used
167 for the imaging experiments. This commercially available radiotracer has a
168 half-life of 109.7 minutes and has been found to behave as an ideal tracer in
169 a range of geologic materials in part because of the charge neutrality of FDG.
170 Fluorodeoxyglucose was diluted in 3 mL of the brine described in Table 1 to
171 reach the optimal radioactivity concentration for minimizing imaging noise [45].
172 Precise control of the radiotracer injection and timing was controlled using a
173 six-port dual-position *VICI Cheminert* HPLC rotary valve with a 3 mL in-
174 jection loop. Pressure and radiation sensors enabled continuous measurement
175 of fluid pressure, pump pressures, and injected radiotracer concentration. To
176 safely handle radioactive liquids, the experimental system utilized extensive lead
177 shielding around the radiation sources.

178 The PET scans were performed using a *Siemens Inveon DPET* pre-clinical
179 scanner at the University of Wisconsin-Madison small animal imaging and radio-
180 therapy facility (SAIRF). Each experiment was completed in 12 hours with four

181 three-hour scans. Due to the length of the experiment, the image timesteps were
182 discretized into 5-minute intervals. However, PET imaging enables timesteps as
183 short as 20 seconds to monitor more rapid transport processes [45]. Sequential
184 PET scans were concatenated together in time by decay correcting to the scan
185 start time [48]. Confirmation of tracer mass balance after image concatenation
186 is illustrated in Figure B.9 in Appendix B. Additional details and theoretical
187 background related to PET imaging experiments in geologic materials are
188 described in previous work [45].

189 *2.4. Low-pH brine injection experimental procedure*

190 Following the first PET scan, the core was exposed to continuous flow-
191 through of pH 4.0 brine analogous to conditions that might occur when brine
192 is saturated with dissolved CO₂. To perform this experiment, the core was
193 again connected to a pump containing the synthetic brine mixture described in
194 Table 1. The experimental setup is illustrated in the upper pane of Figure 1.
195 Brine was injected through the core for a period of seven days (approximately
196 100 mL) to ensure the displacement of any remaining FDG in the core. The
197 injection line of the core was then connected to a piston accumulator (*Parker*
198 *A3NW0058D1E* with a nickel coating) containing the brine solution with the
199 addition of hydrochloric acid (*Baker Analyzed*, assay: 37.1%, density: 2.7 kg/1
200 L). This produced a brine solution with a pH of 4.0 that was then injected
201 continuously at a constant pressure of 2200 kPa (320 psi), backpressure of 1510
202 kPa (220 psi), and confining pressure of 3790 kPa (550 psi) for 21 days. The
203 reacted brine was produced at the outlet. At these conditions, a total of 55.4
204 pore volumes of weakly acidic brine was injected over a period of 21 days.

205 Throughout the pH 4.0 brine injection, the core sleeve was covered with
206 heat tape and insulated to maintain a constant temperature of 40 °C. This
207 temperature regulation was principally employed to more closely represent in
208 situ reservoir conditions. Following the 21 day injection, a second conservative
209 tracer PET scan was performed under identical conditions as the first PET
210 experiment as described in Section 2.3.

211 *2.5. Fracture identification and PET image processing*

212 To quantify fracture-matrix transport, the raw PET scans were segmented
213 into voxels containing fractures and voxels not containing fractures. The raw
214 data was first coarsened by a factor of three, giving a voxel size of $2.3 \text{ mm} \times 2.3$
215 $\text{mm} \times 2.3 \text{ mm}$. Raw images were coarsened by a factor of three by taking the
216 arithmetic average of $3 \times 3 \times 3$ voxels, thereby also reducing the number of voxels
217 by a factor of 27. Coarsening was performed to reduce imaging noise [45] and to
218 ensure that the voxels were large enough to capture the majority of the solute
219 that diffused into the matrix over the duration of the experiment. This voxel size
220 also results in a fracture-to-matrix volume that enables the quantity of the tracer
221 in the fracture to be neglected from analytical model fitting. The radiotracer
222 in the fracture is assumed to be negligible because the fracture apertures were
223 estimated to be in the tens of micrometers or less based on the X-ray CT
224 images and therefore occupied less than one percent of the coarsened voxel
225 volume. Coarsened voxels containing fractures were identified by first applying
226 the Frangi vesselness filter [56]. The Frangi filter has been used to detect image
227 features such as vessels, wrinkles, and rivers [57, 58]. Filtered images were then
228 thresholded to select voxels in the core that most likely correspond to voxels
229 containing fractures.

230 *2.6. Semi-analytical fracture matrix transport model description*

231 Once voxels containing fractures were identified from the PET images, an
232 analytical transport model was fit to each voxel breakthrough curve. An analyt-
233 ical solution was employed that accounts for advection and dispersion along the
234 fracture and diffusion into the matrix [24]. Solute dispersion within the fracture
235 results from mechanisms that drive spatial variability in fluid velocities such
236 as Taylor dispersion, fracture roughness, and aperture variability [59, 60, 61].
237 Fitting the analytical solution to each voxel breakthrough curve enabled the
238 voxel-scale estimation of matrix tortuosity (τ'), local fracture longitudinal dis-
239 persivity (α_z), and local fracture advection velocity (v_z).

The differential equation for solute transport in the fracture is given by

$$\frac{\partial C}{\partial t} - D_z \frac{\partial^2 C}{\partial z^2} + v_z \frac{\partial C}{\partial z} + \frac{q}{b} = 0 \quad (1)$$

240 Here, D_z is the hydrodynamic dispersion coefficient in the fracture that can be
 241 defined by $D_z = \alpha_z v_z + \mathcal{D}$ where \mathcal{D} is the bulk molecular diffusion coefficient in
 242 water. A value of molecular diffusion of $\mathcal{D} = 6.7 \times 10^{-6}$ [cm²/s] was assumed based
 243 on the diffusion coefficient of glucose in water. The variable q is the diffusive
 244 flux perpendicular to the fracture face and b is half of the fracture aperture. The
 245 mean fracture aperture was roughly estimated to be 20 μm using the calibration-
 246 free missing attenuation method [48] on the X-ray CT scan shown in Figure 2.

Advection into the matrix is assumed to be negligible so that solute transport can be described by the diffusion equation.

$$\frac{\partial C'}{\partial t} - D' \frac{\partial^2 C'}{\partial x^2} = 0 \quad (2)$$

247 The notation C' explicitly denotes the concentration of solute in solution in
 248 the matrix following the original notation of Tang et al [24]. The variable D'
 249 is the effective diffusion coefficient in the matrix that is related to the bulk
 250 liquid diffusion coefficient (\mathcal{D}) by $D' = \tau' \mathcal{D}$, where τ' is the matrix tortuosity
 251 [62, 24] or sometimes referred to as the diffusibility [63]. Note that this is
 252 related to another common definition of tortuosity (τ) often found in literature,
 253 sometimes also termed the lithologic factor [62] or matrix factor [63]. This τ
 254 term refers to the distance some particle must travel through a porous media
 255 relative to the straight line distance. These two definitions are related by the
 256 expression $\tau' = \phi/\tau$, where ϕ is the matrix porosity [62, 64, 65]. However other
 257 relationships with porosity have been proposed in literature [63]. For clarity, τ'
 258 will be referred to as the matrix tortuosity throughout this manuscript.

The concentration gradient ($\partial C'/\partial x$) at the fracture-matrix interface is related to the diffusive flux (q) in Equation 1 by the following equation.

$$q = -\theta D' \left. \frac{\partial C'}{\partial x} \right|_{x=b} \quad (3)$$

Equation 3 can then be substituted into Equation 1 to obtain the coupled equation for advection and dispersion in the fracture and orthogonal diffusion into the matrix.

$$\left. \frac{\partial C}{\partial t} - D_z \frac{\partial^2 C}{\partial z^2} + v_z \frac{\partial C}{\partial z} - \frac{\theta D'}{b} \frac{\partial C'}{\partial x} \right|_{x=b} = 0 \quad (4)$$

The solution for matrix concentration (C') at a distance (z) from the inlet of the core, a distance (x) from the center of the fracture as a function time t has been previously derived [24]. Specifically, for the following boundary and initial conditions

$$C(0, t) = C_0 \quad (5)$$

$$C(\infty, t) = 0 \quad (6)$$

$$C(z, 0) = 0 \quad (7)$$

$$C'(b, z, t) = C(z, t) \quad (8)$$

$$C'(\infty, z, t) = 0 \quad (9)$$

$$C'(x, z, 0) = 0 \quad (10)$$

259 the solution for matrix concentration (C') based on the coupled equation is
 260 given by Equation 11. Note that C_0 is the source concentration.

$$\frac{C'}{C_0} = \frac{\exp(\nu z)}{\pi^{1/2}} \int_l^\infty 2 \exp \left[-\xi^2 - \frac{\nu^2 z^2}{4\xi^2} \right] \exp(-\eta z^2) \operatorname{erfc} \left[\frac{Y'}{2T} \right] d\xi \quad (11)$$

Here T and Y' are given by Equation 12 and 13, respectively.

$$T = \sqrt{t - \frac{z^2}{4D_z \xi^2}} \quad (12)$$

$$Y' = \frac{v^2 \beta^2 z^2}{4A \xi^2} + B(x - b) \quad (13)$$

Variables ν and β are defined as $\nu = v/2D_z$ and $\beta = \sqrt{4D_z/v^2}$. The lower limit of the integral (l) in Equation 11 is equal to Equation 14.

$$l = \frac{z}{\sqrt{4D_z t}} \quad (14)$$

261 Additional mathematical derivation details can be found in Tang et al. [24].
262 Note that unlike the original solution in [24], the first-order reaction/decay terms
263 are neglected because all of the reconstructed PET data are decay corrected
264 based on the 109.7 min half-life of ^{18}F .

265 Equation 11 was solved with a two-step composite trapezoidal function pro-
266 grammed in Python. The first step was to determine the upper limit of the
267 integral in Equation 11—below which the integrand is greater than zero. The
268 second step was to then solve the integral between l and this upper limit with
269 a very fine discretization of ξ . This two-step numerical method was found to
270 be more numerically efficient than the Gaussian quadrature method. To fit
271 this equation to the volume-average concentrations in each fracture-containing
272 voxel as a function of time, Equation 2 was solved as a function of distance into
273 the matrix (x) at each time step. This resulted in a concentration profile as
274 a function of distance x from the fracture center to the voxel edge—assuming
275 the fracture was in the middle of the voxel. This profile was then integrated as
276 a function of x from each side of the fracture and divided by the voxel width
277 to calculate the expected average voxel concentration of radiotracer at a given
278 time. To fit the analytical model to the measured breakthrough data, a non-
279 linear least squares fitting routine was developed using SciPy package functions.
280 The processed data and Python codes used for analysis and analytical modeling
281 are available in the data repository cited in the Acknowledgements.

282 *2.7. One-dimensional reactive transport simulation*

283 A multi-component RTM was developed to quantify the extent of fracture-
284 matrix alteration during low pH fluid injection and independently verify the
285 extent of alteration suggested by the experimental results and fracture-matrix
286 transport model. A one-dimensional (1D) RTM was constructed in the open-
287 source numerical reactive transport software CrunchFlow [35]. The RTM tracks
288 changes in mineral volumes resulting from solubilization due to exposure to the
289 through-flowing weakly acidic brine. The initial mineral volumes used for the
290 RTM are given in Table 2. The mineral volumes were determined based on min-

291 eral densities and the weight percents measured in the core and reported in Table
 292 A.3, and rounded to the nearest integer. The starting mineralogy includes pla-
 293 gioclase, specifically albite, and clays including smectite and illite. The injected
 294 fluid chemistry composition is based on the laboratory brine described in Table
 295 1. Mineral reaction kinetics, temperature-dependent equilibrium coefficients,
 296 and multi-component aqueous speciation including the carbonate equilibria and
 297 associated feedbacks to pH, as shown in Table C.4 and C.5, are all included in
 298 the model based on prior Wolfcamp RTM simulations [5, 6, 7].

299 The model domain was oriented to allow transport perpendicular to the
 300 plane of the fracture with one end of the model representing the fracture-matrix
 301 interface and the other end representing the no-flow walls of the core. The
 302 length of the model was 12.6 millimeters long and 1 millimeter wide. The
 303 bulk diffusion of HCl in water is $\mathcal{D} = 5.25\text{e-}5 \text{ cm}^2/\text{sec}$ [66]. To set the model
 304 diffusion, the bulk diffusion was multiplied by $\tau' = 0.0125$. The pressure drop
 305 from the fracture into the matrix was assumed to be low and was set to 6.9 kPa
 306 (1 psi). The temperature was set to 40 °C. The permeability of the matrix was
 307 approximated as $10 \mu\text{D}$ as estimated based on steady-state differential pressure
 308 following core saturation with brine. The starting porosity of the model was
 309 10.2 percent as measured with the X-ray CT scan and identical to the value
 310 used for the analytical transport model. The model input files and database are
 311 available in the data repository cited in the Acknowledgements.

Table 2: Starting mineral volume fractions of the Wolfcamp sample specified in the reactive transport simulation.

Mineral	Quartz	K-Feldspar	Albite	Calcite	Dolomite	Pyrite	Illite	Smectite
vol%	57	1	4	0	3	1	22	1

312 **3. Results**

313 *3.1. Fracture identification and concentration quantification with PET imaging*

314 The core and fracture geometry is illustrated in the X-ray CT scan in Figure
315 2. The CT scan depicts one nearly through-going bedding-parallel fracture that
316 intersects the inlet face of the core. There are several other small microfractures
317 semi-parallel to this main fracture, including several that intersect the outlet
318 face of the core. The results of the radiotracer injection and imaging with PET
319 prior to acid exposure are illustrated in Figure 3. The red shading indicates
320 radiotracer concentration in uncoarsened PET images in different slices along
321 the axis of the core. The PET images clearly show the transport of radiotracer
322 through these fractures identified in the X-ray CT scan.

323 Radiotracer injection and imaging before and after acid exposure are shown
324 in Figures 3 and 4, respectively. Results of the coarsened and thresholded voxels
325 containing fractures are highlighted by the grey shading in Figure 3 (pre-acid in-
326 jection) and Figure 4 (post-acid injection). The threshold was selected such that
327 there was a very high degree of confidence that the voxel contained the fracture
328 and was not influenced by core boundary conditions. As a result, many vox-
329 els that likely contained fractures were neglected from the analytical parameter
330 fitting. Regardless of these neglected voxels, there were 156 voxels thresholded
331 in the pre-acid scan and 153 voxels thresholded in the post-acid scan. Note
332 that while many of these voxels were in identical locations as can be seen by
333 comparing Figures 3 and 4, the thresholding workflow did not include a routine
334 to select identical sets of fracture-containing voxels due to subtle differences in
335 image registration between the scans.

336 *3.2. Voxel-scale transport quantification*

337 Figures 5 and 6 show the results of fitting the analytical model (right plots)
338 to the fracture-containing voxel breakthrough curves (left plots) before and af-
339 ter low-pH brine injection, respectively. The initial breakthrough of tracer in
340 different voxels varied as a function of position along the length of the fracture.

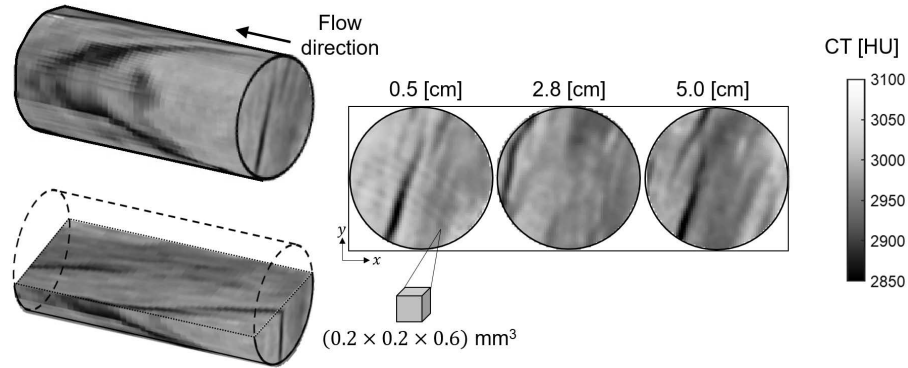


Figure 2: X-ray CT image of the Wolfcamp shale core. The two-dimensional slices illustrated on the right highlight the geometry of the fracture (darker regions) prior to low-pH fluid injection. The slices are taken at increasing distances from the inlet ($z=0$). The grey colorscale in all images is in Hounsfield units [HU].

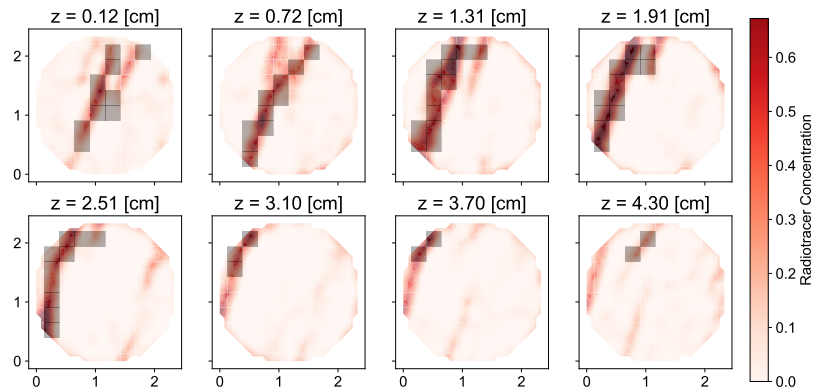


Figure 3: Two-dimensional slices through the core in the PET scan prior to acid exposure after 144 minutes of tracer injection. The slices are at increasing distances from the inlet ($z=0$). X and Y axes are length scales in centimeters. The red color scale illustrates the radiotracer concentration and the shaded grey boxes highlight the thresholded voxels used for fitting the analytical transport model.

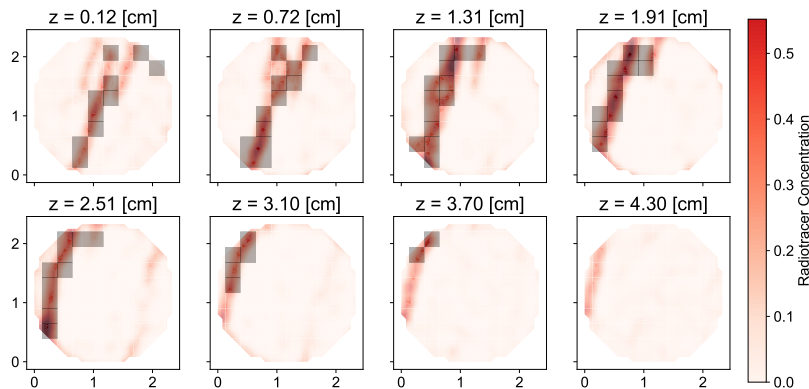


Figure 4: Two-dimensional slices through the core in the PET scan after acid exposure after 143 minutes of tracer injection. The slices are at increasing distances from the inlet ($z=0$). X and Y axes are length scales in centimeters. The red color scale gives radiotracer concentration and the shaded grey boxes highlight the coarsened thresholded voxels used for fitting the analytical transport model.

341 The line colors in Figures 5 and 6 are based on voxel distance from the inlet
 342 of the core. In all voxels, the matrix tortuosity, fracture dispersivity, and frac-
 343 ture advection velocity were determined by fitting the analytical model to the
 344 breakthrough curves in the voxels containing fractures. It is clear from these
 345 figures that the analytical model was able to capture the trends in the measured
 346 concentrations despite the simplifying assumptions of the analytical model.

347 Statistical distributions of the fit parameters from the tracer tests before
 348 and after low-pH brine injection are illustrated in the histograms in Figure 7.
 349 The histogram of matrix tortuosity values indicates that there is a slight shift
 350 toward higher matrix tortuosity and therefore higher effective matrix diffusion
 351 following low-pH brine injection—with the mean matrix tortuosity increasing
 352 from 0.038 to 0.040. The histogram of fracture dispersivity indicates that dis-
 353 persivity is slightly higher following acid exposure and the fracture advection
 354 velocity is slightly lower and has a more uniformly distributed following low-pH
 355 brine injection.

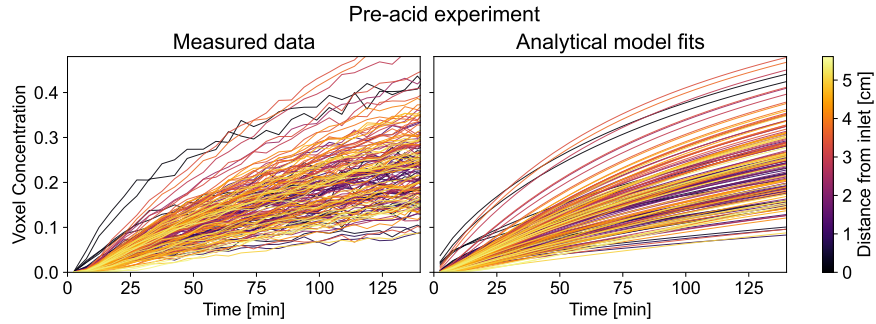


Figure 5: (left) Breakthrough curves for every voxel in the fracture determined from the PET scan prior to low-pH brine injection, as determined from the Frangi filter segmentation method described in Section 2.5. (right) Corresponding analytical fits to each voxel breakthrough curve. The colors in the analytical fit correspond to the same color of each voxel of measured data. The line color corresponds to the approximate distance from the inlet of the core in centimeters as described by the colorbar.

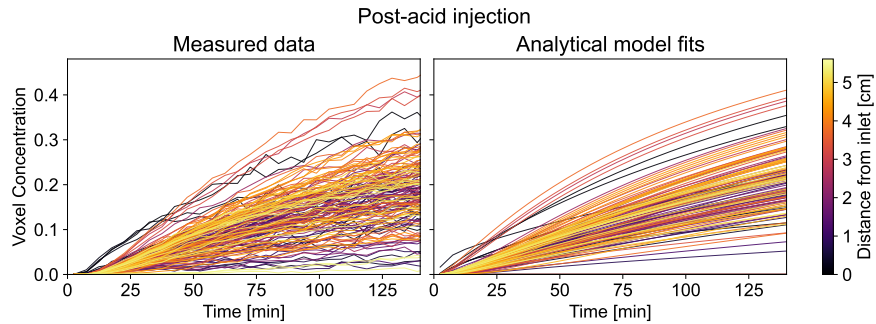


Figure 6: (left) Breakthrough curves for every voxel measured in the fracture using the PET scan taken after low-pH brine injection. (right) Corresponding analytical fits to each voxel breakthrough curve. The colors in the analytical fit correspond to the same color of each voxel of measured data. The line color corresponds to the approximate distance from the inlet of the core in centimeters as indicated by the colorbar.

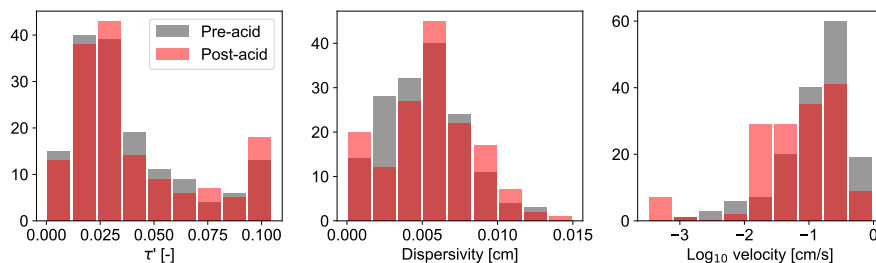


Figure 7: Histogram of fit matrix tortuosity values (left) describing matrix diffusion, fracture dispersivity (center), and fracture advection velocity (right) before and after low-pH brine injection—indicated by grey and red shading, respectively.

356 *3.3. One-dimensional reactive transport simulations of acidified fluid injection*

357 The results of the 1D reactive transport simulation described in Section 2.7
 358 are illustrated in Figure 8. The transport of reactive species within the matrix
 359 is almost entirely driven by diffusion. The results illustrate increasing porosity
 360 at the fracture-matrix interface caused by the rapid dissolution of dolomite
 361 as a function of injection time. Due to the reactivity of carbonate minerals,
 362 the dissolution front only progresses away from the fracture after all dolomite
 363 minerals have been dissolved. While these carbonates are still present, the
 364 acid is neutralized and reactivity is arrested. If reactive fluid injection was
 365 conducted for a longer period of time or with lower pH-brine, dissolution of
 366 additional minerals such as K-feldspar, albite, smectite, and pyrite would lead
 367 to further porosity reduction over longer timescales as illustrated by the small
 368 volume changes of these minerals in the plots in Appendix C. As noted in
 369 Section 2.1, pyrite oxidation is assumed to be minimal because the sample was
 370 vacuumed and purged with CO₂ prior to saturating with brine that was purged
 371 with nitrogen gas prior to injection.

372 **4. Discussion**

373 The workflow of PET imaging, fracture-containing-voxel segmentation, and
 374 analytical model fitting demonstrates one of the first direct approaches for

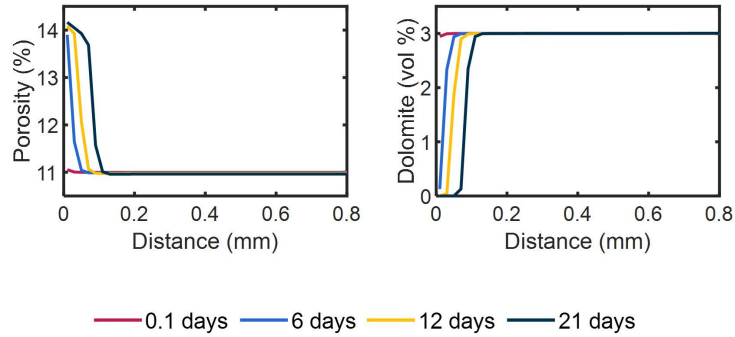


Figure 8: (Left) Model results of predicted porosity increase as a function of distance perpendicular to the fracture-matrix interface over a period of 21 days. (Right) Model output describing the reduction in dolomite volume in the matrix at increasing distance from the fracture-matrix interface due to dissolution.

375 millimeter-scale quantification of solute transport throughout a centimeter-scale
 376 shale core sample. This provides new insights into the distribution of parameters
 377 associated with transport through complex fracture geometry and diffusion into
 378 a spatially heterogeneous matrix. While a number of analytical solutions exist
 379 for describing the extent of fracture-matrix transport, the solution of Tang et al
 380 [24] is most applicable to the estimation of transport in the naturally fractured
 381 shale sample where advection in the matrix can be assumed to be negligible
 382 and the solute concentration in the fracture can not be assumed to be con-
 383 stant. Other analytical models could be substituted into this type of workflow
 384 based on the extent of matrix advection or differences in experimental boundary
 385 conditions or initial conditions.

386 The matrix tortuosity results in Figure 7 further justify the application of
 387 this analytical model which assumes that the vast majority of the tracer stays
 388 within the fracture-containing voxels over the time period of the model fit (144
 389 minutes). Integrating the solution to the diffusion equation with respect to
 390 distance and using upper 80th percentile matrix tortuosity of $\tau' = 0.058$ in-
 391 dicates that 90.6% of the tracer would diffuse a distance less than half of the
 392 distance of the voxel size of 0.23 cm. At the median matrix tortuosity post-acid

393 of $\tau' = 0.029$, 97.5% of the tracer would diffuse a distance less than the voxel
394 half-length.

395 The matrix tortuosity values calculated with this method also agree well with
396 values from literature measured in similar rocks and at similar spatial scales.
397 Published matrix tortuosity values at similar spatial scales are the most directly
398 comparable as reviews of previous studies have observed scale dependence in
399 field measurements [67], similar to the scale dependence observed for dispersion
400 [68]. At the laboratory scale, the typical approach for the quantification of
401 diffusion relies on bulk measurements of gas diffusion into or through samples
402 and corresponding analytical model fits [69, 70, 64, 71]. The methods in this
403 study are analogous to these approaches with the exception that an analytical
404 model can be applied to every voxel of the image-based data, as opposed to
405 typical bulk sample-average measurements. This image-based method results in
406 hundreds of measurements of matrix tortuosity in a given sample. Measurements
407 of matrix tortuosity reported in previous studies of low permeability samples
408 include low permeability limestones 0.031-0.051 [62], a clay-rich marl 0.005 [70],
409 and other low permeability samples where lithology was not specified 0.0082
410 [64], 0.004 - 0.01 [72]. In an extensive study of light hydrocarbon diffusion
411 in sedimentary rocks, Krooss and Leythaeuser [69, 73] measured bulk matrix
412 tortuosity values ranging from 0.002 to 0.077 with a mean of 0.036 in ten different
413 siltstone and shale samples. Thus, the image-based approach for local diffusion
414 and matrix tortuosity quantification in this study agrees well with previous
415 results in rocks of similar lithology.

416 The local advection rates calculated from the analytical fitting range from
417 0.001 cm/s to 0.6 cm/s in the pre-acid experiments and from 0.0007 cm/s to 0.5
418 cm/s in the post-acid experiments. The mean pre-acid advection velocity is 0.2
419 cm/s while the mean post-acid advection velocity was 0.14 cm/s. These mean
420 velocities would suggest a mean fracture aperture of around four micrometers
421 based on an injection rate of 0.013 mL/min and assuming a single fracture that
422 is 2.54 cm wide—the same width as the core. These values are reasonable given
423 the micro-Darcy permeability of the shale core, the presence of channelized

424 flow within fractures that is apparent in the PET images, and the complexity
425 of flow and transport between multiple fractures along the axis of the core.
426 Note however that the calculated dispersivity and advection velocity values are
427 strongly dependent on a relatively small number of early-time concentration
428 measurements and analytical model assumptions about the linear distance of
429 the voxel from the inlet of the core. Therefore these parameters are more prone
430 to model fitting errors than the matrix tortuosity values that are constrained
431 by a larger number of long-time concentration measurements reflecting fracture-
432 matrix diffusion.

433 The reactive transport simulations independently support the experimen-
434 tal image-based observations, suggesting that acid exposure could enhance the
435 porosity of the matrix near the fracture-matrix interface—depending on the lo-
436 cal mineralogical carbonate content. Specifically, the dissolution of dolomite in
437 the matrix shown in the right plot of Figure 8 corresponds to a subtle increase in
438 porosity shown in the left plot of Figure 8 at the fracture-matrix interface. This
439 dissolution is consistent with the slight increase in the matrix tortuosity follow-
440 ing acid exposure. However as shown in the left plot in Figure 7, this increase
441 in tortuosity is not widespread and seems to be restricted to small subregions
442 of the fractures.

443 In addition to enhanced connectivity, previous studies have shown that
444 extended matrix exposure to acidic pH conditions results in shale softening
445 [74, 75, 6]. Low pH conditions drive reactions in mineralogically heterogeneous
446 shales that have been observed to increase surface roughness, drive fines mi-
447 gration, and induce clay swelling [6]. Our observations of an approximately
448 linear permeability reduction from $15 \mu\text{D}$ to $7 \mu\text{D}$ over the course of the 21 day
449 pH 4.0 brine injection experiment, combined with the more uniform advection
450 velocities after low-pH brine injection shown in Figure 7, suggest reduced flow
451 channelization and softening at the fracture-matrix interface. It is also possible
452 that there was some mechanical deformation to fracture asperities due to pres-
453 surizing and depressurizing the confining pressure on the core during transport
454 between imaging facilities.

455 **5. Conclusion**

456 In this study, slug tracer experiments were performed in a naturally fractured
457 Wolfcamp shale core and imaged with positron emission tomography before
458 and after 21 days of injection of a low pH brine. Imaging results were used
459 to quantify fracture-matrix transport by fitting a solution to the advection-
460 dispersion equation [24]. This image-based transport quantification enabled the
461 local voxel-level determination of matrix tortuosity, fracture dispersivity, and
462 local advection velocity in over 150 unique locations throughout the core sample.
463 Distributions of local tortuosity and fracture advection velocity distributions,
464 combined with 1D reactive transport simulations, indicate subtle changes in
465 diffusivity and likely shale softening at the fracture-matrix interface. This shale
466 softening and reduced channelization led to lower permeability and reduced
467 fracture channelization following exposure to low pH conditions.

468 The experimental imaging workflow and transport parameterization demon-
469 strated in this study provides a new approach for understanding the spatial
470 and temporal evolution of flow and transport behavior in naturally fractured
471 core samples. These multiscale observations and models improve mechanistic
472 understanding and scale translation of flow and reactive transport processes in
473 shale formations in response to transient changes in pore fluid chemistry. This
474 understanding is key for the management of groundwater resources, storage se-
475 curity of geologically sequestered CO₂, resource recovery following hydraulic
476 fracturing, and long-term nuclear waste repository design.

477 **Acknowledgements**

478 Datasets and analytical modeling and analysis codes are available at the
479 Stanford Data Repository [76]. The experimental system used for column and
480 imaging experiments was supported by the National Science Foundation under
481 Grant No. 2002412. Any opinions, findings, and conclusions or recommenda-
482 tions expressed in this material are those of the authors and do not necessarily
483 reflect the views of the National Science Foundation. This work was supported

484 as part of the Center for Mechanistic Control of Unconventional Formations
 485 (CMC-UF), an Energy Frontier Research Center funded by the U.S. Department
 486 of Energy, Office of Science under DOE (BES) Award DE-SC0019165. Further
 487 support for this research was provided by the Office of the Vice Chancellor for
 488 Research and Graduate Education at the University of Wisconsin-Madison with
 489 funding from the Wisconsin Alumni Research Foundation.

490 **Appendix A. Shale sample mineral composition**

491 Table A.3 summarizes the mineral composition in weight percentage of the
 492 Wolfcamp sample used in the experiments.

Table A.3: Mineral composition of the Wolfcamp sample.

Mineral	Quartz	K-Feldspar	Plagioclase	Calcite	Dolomite	Pyrite	Illite	Mixed Illite/Smectite	Organic Matter
wt%	62.1	0.8	4.8	0.2	3.7	2.6	19.4	6.4	2.7

493 **Appendix B. Concatenating multiple PET scans**

494 Figure B.9 illustrates the PET scan concatenation and decay correction back
 495 to the beginning of the first scan. Our recent work verified that radioactivity
 496 is conserved across multiple scans after decay correction [48]. The uncorrected
 497 (dashed line) in Figure B.9 also illustrates how the signal from the radiotracer
 498 decreases through time due to the radioactive decay of the 110-minute half-life
 499 ^{18}F radioisotope.

500 **Appendix C. Reactive transport results for non carbonate species**

501 Table C.4 and C.5 show the aqueous reactions and mineral kinetic reactions
 502 respectively. Aqueous kinetic reactions respect a rate-dependent transition state
 503 theory (TST) rate law as shown in Equation C.1 [77] where $\prod (a_i)^n$ indicates
 504 the product of rate dependency on all aqueous species, K_{eq} refers to equilibrium

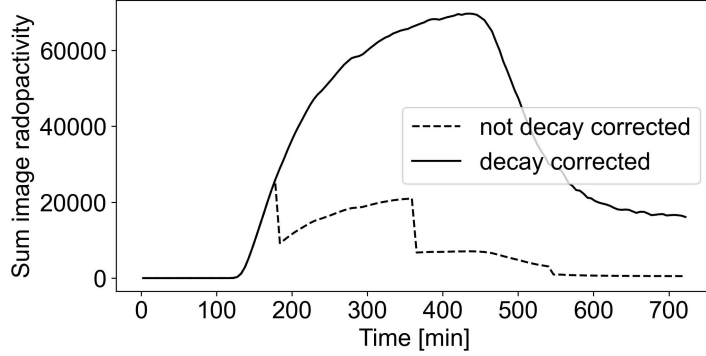


Figure B.9: Total activity in core as a function of time in PET scan prior to acidified brine injection.

505 constant, k is the reaction rate constant in $\text{mol}(\text{kg water})^{-1}\text{yr}^{-1}$, and IAP is
 506 the ion activity product.

$$R = k \prod (a_i)^n \left[1 - \frac{\text{IAP}}{K_{eq}}\right] \quad (\text{C.1})$$

507 Mineral dissolution and precipitation also respect a TST rate law as shown
 508 in Equation C.2 [77] where $\prod (a_i)^n$ shows rate dependency on species a , K_{sp}
 509 refers to solubility product of the mineral, k is the rate constant in $\text{mol}\cdot\text{m}^{-2}\text{s}^{-1}$,
 510 A_m is mineral surface area in m^2s^{-1} , and IAP is the ion activity product. Tem-
 511 perature dependence of the rate constants are accounted for by the CrunchFlow
 512 numerical simulator using the Arrhenius equation. A_m is set to one for pre-
 513 existing minerals and set to 0.1 for secondary minerals that may precipitate
 514 such as gypsum, halite, $\text{Fe}(\text{OH})_3$, and amorphous SiO_2 .

$$R = A_m k \prod (a_i)^n \left[1 - \frac{\text{IAP}}{K_{eq}}\right] \quad (\text{C.2})$$

515 Additional observations from the reactive transport model suggest volume
 516 reduction of K-feldspar, albite, pyrite, and smectite with time due to dissolu-
 517 tion that occurs at a significantly lower rate than carbonates (Figure C.10).
 518 These plots show that the precipitation of pyrite is followed immediately after
 519 dissolution.

Table C.4: Instantaneous aqueous speciation reactions considered in the reactive transport model. The equilibrium constants are reported for 40°C and derived from Li et al [78].

Equilibrium Reactions [78]	$\log_{10}(K_{eq})$ [78]
$\text{Fe}^{3+} + 0.5\text{H}_2\text{O} \leftrightarrow \text{Fe}^{2+} + \text{H}^+ + 0.25\text{O}_2(\text{aq})$	-7.66
$\text{AlOH}^{2+} + \text{H}^+ \leftrightarrow \text{Al}^{3+} + \text{H}_2\text{O}$	4.53
$\text{Al}(\text{OH})_2^+ + 2\text{H}^+ \leftrightarrow \text{Al}^{3+} + 2\text{H}_2\text{O}$	9.76
$\text{Al}(\text{SO})_4^+ \leftrightarrow \text{SO}_4^{2-} + \text{Al}^{3+}$	-3.01
$\text{MgCl}^+ \leftrightarrow \text{Cl}^- + \text{Mg}^{2+}$	0.12
$\text{H}_2\text{S}(\text{aq}) \leftrightarrow \text{H}^+ + \text{HS}^-$	-6.81
$\text{H}_2\text{SO}_4(\text{aq}) \leftrightarrow 2\text{H}^+ + \text{SO}_4^{2-}$	1.02
$\text{HSO}_4^- \leftrightarrow \text{H}^+ + \text{SO}_4^{2-}$	-2.14
$\text{CaCl}^+ \leftrightarrow \text{Ca}^{2+} + \text{Cl}^-$	0.67
$\text{CaCl}_2(\text{aq}) \leftrightarrow \text{Ca}^{2+} + 2\text{Cl}^-$	0.67
$\text{CaOH}^+ + \text{H}^+ \leftrightarrow \text{Ca}^{2+} + \text{H}_2\text{O}$	12.9
$\text{CaSO}_4(\text{aq}) \leftrightarrow \text{Ca}^{2+} + \text{SO}_4^{2-}$	-2.16
$\text{HCl}(\text{aq}) \leftrightarrow \text{H}^+ + \text{Cl}^-$	-0.69
$\text{H}^+ + \text{OH}^- \leftrightarrow \text{H}_2\text{O}$	13.54
$\text{CO}_2(\text{aq}) + \text{H}_2\text{O} \leftrightarrow \text{H}^+ + \text{HCO}_3^-$	-6.28
$\text{CO}_3^{2-} + \text{H}^+ \leftrightarrow \text{HCO}_3^-$	10.22

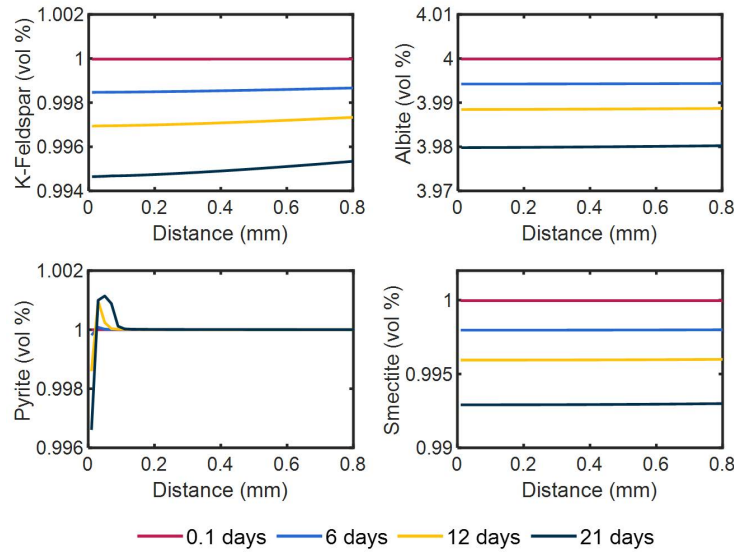


Figure C.10: Volume reductions of K-feldspar (upper left), albite (upper right), pyrite (lower left), and smectite (lower right) indicate slow dissolution of these minerals at the fracture-matrix interface.

Table C.5: Mineral kinetic reactions and their model parameters. $\prod(a_i)^n$ shows rate dependency on species a, $\log_{10}(K_{sp})$ is solubility product of minerals at 40°C and $\log_{10}(k)$ is the rate constant in $\text{mol}\cdot\text{m}^{-2}\text{s}^{-1}$ shown for 25°C.

Minerals	Reactions [78]	$\prod(a_i)^n$ [78]	$\log_{10}(K_{sp})$ [78]	$\log_{10}(k)$
Quartz	Quartz \leftrightarrow SiO ₂ (aq)	None	-3.74	-15[78]
K-Feldspar	K-Feldspar + 4H ⁺ \leftrightarrow Al ³⁺ + K ⁺ + 2H ₂ O + 3SiO ₂ (aq)	None	-0.53	-11.5[79]
Albite	Albite + 4H ⁺ \leftrightarrow Al ³⁺ + Na ⁺ + 2H ₂ O + 3SiO ₂ (aq)	None	2.27	-11.5[80, 81]
Calcite	Calcite + H ⁺ \leftrightarrow Ca ²⁺ + HCO ₃ ⁻	(H ⁺) ^{1.0}	1.63	-3.5[78]
Dolomite	Dolomite + 2H ⁺ \leftrightarrow Ca ²⁺ + Mg ²⁺ + 2HCO ₃ ⁻	(H ⁺) ^{0.5} , None	2.0	-7.7[78]
Pyrite	Pyrite + H ₂ O \leftrightarrow Fe ²⁺ + 1.75HS ⁻ + 0.25SO ₄ ²⁻ + 0.25H ⁺	None	-23.75	-7.5[80, 82]
Illite	Illite + 8H ⁺ \leftrightarrow 0.25Mg ²⁺ + 0.6K ⁺ + 2.3Al ³⁺ + 3.5SiO ₂ (aq) + 5H ₂ O	None	7.51	-11[78]
Smectite	Smectite + 7H ⁺ \leftrightarrow 0.02Ca ²⁺ + 0.15Na ⁺ + 0.16Fe ³⁺ + 0.2K ⁺ + 0.29Fe ³⁺ + 0.9Mg ²⁺ + 1.25Al ³⁺ + 3.75SiO ₂ (aq)	None	8.53	-11[80, 83]
Gypsum	Gypsum \leftrightarrow Ca ²⁺ + SO ₄ ²⁻	None	-4.51	-30[78]
Halite	Halite \leftrightarrow Na ⁺ + Cl ⁻	None	1.61	-0.21[80, 84]
Fe(OH) ₃	Fe(OH) ₃ + 3H ⁺ \leftrightarrow Fe ³⁺ + 3H ₂ O	(H ⁺) ^{1.0}	-5.30	-8.5[78]
SiO ₂ (am)	SiO ₂ (am) \leftrightarrow SiO ₂ (aq)	None	-2.56	-8[78]

520 **References**

- 521 [1] A. Vengosh, R. B. Jackson, N. Warner, T. H. Darrah, A. Kondash, A
522 critical review of the risks to water resources from unconventional shale gas
523 development and hydraulic fracturing in the United States, *Environmental*
524 *Science and Technology* 48 (15) (2014) 8334–8348. doi:10.1021/es405118y.
- 525 [2] M. A. Ferno, L. P. Hauge, A. Uno Rognmo, J. Gauteplass, A. Graue, M. A.
526 Fernø, L. P. Hauge, A. Uno Rognmo, J. Gauteplass, A. Graue, Flow visual-
527 ization of CO₂ in tight shale formations at reservoir conditions, *Geophysical*
528 *Research Letters* 42 (18) (2015) 7414–7419. doi:10.1002/2015GL065100.
529 URL <http://doi.wiley.com/10.1002/2015GL065100>
- 530 [3] C. Zahasky, S. Benson, Evaluation of hydraulic controls for leakage inter-
531 vention in carbon storage reservoirs, *International Journal of Greenhouse*
532 *Gas Control* 47 (2016) 86–100. doi:10.1016/j.ijggc.2016.01.035.
- 533 [4] Q. C. Wenning, C. Madonna, T. Kurotori, C. Petrini, J. Hwang, A. Zap-
534 ponne, S. Wiemer, D. Giardini, R. Pini, Chemo-Mechanical Coupling in
535 Fractured Shale With Water and Hydrocarbon Flow, *Geophysical Research*
536 *Letters* 48 (5) (2021) 0–12. doi:10.1029/2020GL091357.
- 537 [5] Q. Li, A. D. Jew, A. Kohli, K. Maher, G. E. Brown, J. R. Bargar, Thick-
538 nesses of Chemically Altered Zones in Shale Matrices Resulting from Inter-
539 actions with Hydraulic Fracturing Fluid, *Energy and Fuels* 33 (8) (2019)
540 6878–6889. doi:10.1021/acs.energyfuels.8b04527.
- 541 [6] H. J. Khan, E. Spielman-Sun, A. D. Jew, J. Bargar, A. Kavscek, J. L.
542 Druhan, A Critical Review of the Physicochemical Impacts of Water Chem-
543 istry on Shale in Hydraulic Fracturing Systems, *Environmental Science and*
544 *Technology* 55 (3) (2021) 1377–1394. doi:10.1021/acs.est.0c04901.
- 545 [7] B. F. Esteves, E. Spielman-Sun, Q. Li, A. D. Jew, J. R. Bargar, J. L.
546 Druhan, Geochemical modeling of celestite (srso₄) precipitation and reac-

- 547 tive transport in shales, *Environmental Science & Technology* 56 (7) (2022)
548 4336–4344.
- 549 [8] D. Sassani, C. Stone, F. Hansen, E. Hardin, T. Dewers, M. Martinez,
550 R. Rechar, S. Sobolik, G. Freeze, R. Cygan, K. Gaither, J. Holland,
551 P. Brady, Shale disposal of U.S. high-level radioactive waste., Tech. Rep.
552 May, Sandia National Laboratories (SNL), Albuquerque, NM, and Liver-
553 more, CA (United States) (may 2010). doi:10.2172/992338.
554 URL <https://www.osti.gov/servlets/purl/992338/>
- 555 [9] L. F. Orellana, C. Giorgetti, M. Violay, Contrasting me-
556 chanical and hydraulic properties of wet and dry fault
557 zones in a proposed shale-hosted nuclear waste reposi-
558 tory, *Geophysical Research Letters* 46 (3) (2019) 1357–1366.
559 arXiv:<https://agupubs.onlinelibrary.wiley.com/doi/pdf/10.1029/2018GL080384>,
560 doi:<https://doi.org/10.1029/2018GL080384>.
561 URL <https://agupubs.onlinelibrary.wiley.com/doi/abs/10.1029/2018GL080384>
- 562 [10] J. Warren, P. Root, The Behavior of Naturally Fractured Reservoirs, *Soci-*
563 *ety of Petroleum Engineers Journal* 3 (03) (1963) 245–255. doi:10.2118/426-
564 pa.
- 565 [11] K. Pruess, T. N. Narasimhan, A Practical Method for
566 Modeling Fluid and Heat Flow in Fractured Porous Me-
567 dia, *Society of Petroleum Engineers Journal* 25 (01)
568 (1985) 14–26. arXiv:[https://onepetro.org/spejournal/article-](https://onepetro.org/spejournal/article-pdf/25/01/14/2647668/spe-10509-pa.pdf)
569 [pdf/25/01/14/2647668/spe-10509-pa.pdf](https://onepetro.org/spejournal/article-pdf/25/01/14/2647668/spe-10509-pa.pdf), doi:10.2118/10509-PA.
570 URL <https://doi.org/10.2118/10509-PA>
- 571 [12] B. Berkowitz, J. Bear, C. Braester, Continuum models for contaminant
572 transport in fractured porous formations, *Water Resources Research* 24 (8)
573 (1988) 1225–1236. doi:10.1029/WR024i008p01225.
- 574 [13] H. H. Gerke, M. van Genuchten, Dual porosity model for simulating the

- 575 preferential movement of water and solutes in structured porous media, *Water*
576 *Resources Research* 29 (2) (1993) 305–319.
- 577 [14] B. W. Arnold, H. Zhang, A. M. Parsons, Effective-porosity and dual-
578 porosity approaches to solute transport in the saturated zone at yucca
579 mountain: Implications for repository performance assessment, *Geophysical*
580 *Monograph Series* 122 (2000) 313–322. doi:10.1029/GM122p0313.
- 581 [15] J. D. Hyman, S. Karra, N. Makedonska, C. W. Gable, S. L. Painter, H. S.
582 Viswanathan, DfnWorks: A discrete fracture network framework for mod-
583 eling subsurface flow and transport, *Computers and Geosciences* 84 (2015)
584 10–19. doi:10.1016/j.cageo.2015.08.001.
585 URL <http://dx.doi.org/10.1016/j.cageo.2015.08.001>
- 586 [16] C. R. Romano, R. T. Williams, Evolution of Fault-Zone Hydromechanical
587 Properties in Response to Different Cementation Processes, *Lithosphere*
588 2022 (1) (2022). doi:10.2113/2022/1069843.
- 589 [17] M. B. Cardenas, D. T. Slotke, R. A. Ketcham, J. M. S. Jr, Navier-
590 Stokes flow and transport simulations using real fractures shows heavy
591 tailing due to eddies, *Geophysical Research Letters* 34 (July) (2007) 1–6.
592 doi:10.1029/2007GL030545.
- 593 [18] S. Yoon, P. K. Kang, Roughness, inertia, and diffusion effects on anoma-
594 lous transport in rough channel flows, *Physical Review Fluids* 6 (1) (2021)
595 14502. doi:10.1103/PhysRevFluids.6.014502.
596 URL <https://doi.org/10.1103/PhysRevFluids.6.014502>
- 597 [19] C. Soulaïne, P. Creux, H. A. Tchelepi, Micro-continuum Framework for
598 Pore-Scale Multiphase Fluid Transport in Shale Formations, *Transport in*
599 *Porous Media* 127 (1) (2019) 85–112. doi:10.1007/s11242-018-1181-4.
600 URL <https://doi.org/10.1007/s11242-018-1181-4>
- 601 [20] Q. Zhang, H. Deng, Y. Dong, S. Molins, X. Li, C. Steefel, Investigation
602 of Coupled Processes in Fractures and the Bordering Matrix via a Micro-

- 603 Continuum Reactive Transport Model, *Water Resources Research* 58 (2)
604 (2022) 1–18. doi:10.1029/2021WR030578.
- 605 [21] I. Neretnieks, Diffusion in the rock matrix: An important factor in radionu-
606 clide retardation?, *Journal of Geophysical Research* 85 (B8) (1980) 4379.
607 doi:10.1029/JB085iB08p04379.
- 608 [22] B. Berkowitz, J. Zhou, Reactive solute transport in a single fracture, *Water*
609 *Resources Research* 32 (4) (1996) 901–913. doi:10.1029/95WR03615.
- 610 [23] M. T. V. Genuchten, W. J. Alves, Analytical Solutions of the 1D
611 Convective-Dispersive Solute Transport Equation, Tech. Rep. 1661, U.S.
612 Department of Agriculture, Beltsville, MD (1982).
- 613 [24] D. H. Tang, E. O. Frind, E. A. Sudicky, Contaminant transport in fractured
614 porous media: Analytical solution for a single fracture, *Water Resources*
615 *Research* 17 (3) (1981) 555–564. doi:10.1029/WR017i003p00555.
616 URL <http://doi.wiley.com/10.1029/WR017i003p00555>
- 617 [25] D. Roubinet, J. R. De Dreuzy, D. M. Tartakovsky, Semi-analytical solu-
618 tions for solute transport and exchange in fractured porous media, *Water*
619 *Resources Research* 48 (1) (2012) 1–10. doi:10.1029/2011WR011168.
- 620 [26] G. Dávila, L. Luquot, J. M. Soler, J. Cama, 2D reactive transport mod-
621 eling of the interaction between a marl and a CO₂-rich sulfate solution
622 under supercritical CO₂ conditions, *International Journal of Greenhouse*
623 *Gas Control* 54 (2016) 145–159. doi:10.1016/j.ijggc.2016.08.033.
624 URL <http://dx.doi.org/10.1016/j.ijggc.2016.08.033>
- 625 [27] H. Deng, M. Voltolini, S. Molins, C. Steefel, D. DePaolo, J. Ajo-Franklin,
626 L. Yang, Alteration and Erosion of Rock Matrix Bordering a Carbonate-
627 Rich Shale Fracture, *Environmental Science and Technology* 51 (15) (2017)
628 8861–8868. doi:10.1021/acs.est.7b02063.
- 629 [28] A. D. Jew, J. L. Druhan, M. Ihme, A. R. Kovscek, I. Battiato, J. P.
630 Kaszuba, J. R. Bargar, G. E. Brown Jr, Chemical and reactive transport

- 631 processes associated with hydraulic fracturing of unconventional oil/gas
632 shales, *Chemical reviews* 122 (9) (2022) 9198–9263.
- 633 [29] Y. Zhang, P. Mostaghimi, A. Fogden, A. Sheppard, A. Arena, J. Middleton,
634 R. T. Armstrong, Time-Lapsed Visualization and Characterization of Shale
635 Diffusion Properties Using 4D X-ray Microcomputed Tomography, *Energy
636 and Fuels* 32 (3) (2018) 2889–2900. doi:10.1021/acs.energyfuels.7b03191.
- 637 [30] C. I. Steefel, K. T. MacQuarrie, Approaches to modeling of reactive trans-
638 port in porous media, *Reactive transport in porous media* (2018) 83–130.
- 639 [31] J. M. Galíndez, J. Molinero, Assessment of the long-term stability of ce-
640 mentitious barriers of radioactive waste repositories by using digital-image-
641 based microstructure generation and reactive transport modelling, *Cement
642 and Concrete Research* 40 (8) (2010) 1278–1289.
- 643 [32] M. Xie, K. U. Mayer, F. Claret, P. Alt-Epping, D. Jacques, C. Steefel,
644 C. Chiaberge, J. Simunek, Implementation and evaluation of permeability-
645 porosity and tortuosity-porosity relationships linked to mineral dissolution-
646 precipitation, *Computational Geosciences* 19 (3) (2015) 655–671.
- 647 [33] K. T. MacQuarrie, K. U. Mayer, Reactive transport modeling in fractured
648 rock: A state-of-the-science review, *Earth Science Reviews* 72 (3-4) (2005)
649 189–227.
- 650 [34] C. I. Steefel, D. J. DePaolo, P. C. Lichtner, Earth and planetary science
651 letters, *Reactive transport in porous media* (3-4) (2005) 539–558.
- 652 [35] C. Steefel, C. Appelo, B. Arora, D. Jacques, T. Kalbacher, O. Kolditz,
653 V. Lagneau, P. Lichtner, K. U. Mayer, J. Meeussen, et al., Reactive trans-
654 port codes for subsurface environmental simulation, *Computational Geo-
655 sciences* 19 (3) (2015) 445–478.
- 656 [36] J. Druhan, C. Tournassat, M. S. of Mineralogical Society of America, Re-
657 active transport in natural and engineered systems, Vol. 85, Mineralogical
658 Society of America, 2019.

- 659 [37] H. J. Khan, C. M. Ross, J. L. Druhan, Impact of concurrent solubiliza-
660 tion and fines migration on fracture aperture growth in shales during
661 acidized brine injection, *Energy & Fuels* 36 (11) (2022) 5681–5694.
662 doi:<https://doi.org/10.1021/acs.energyfuels.2c00611>.
663 URL <https://pubs.acs.org/doi/full/10.1021/acs.energyfuels.2c00611>
- 664 [38] M. H. Bradbury, A. Green, Measurement of important parameters de-
665 termining aqueous phase diffusion rates through crystalline rock ma-
666 trices, *Journal of Hydrology* 82 (1-2) (1985) 39–55. doi:10.1016/0022-
667 1694(85)90045-9.
- 668 [39] K. Skagius, I. Neretnieks, Diffusivity Measurements and Electrical Resis-
669 tivity Measurements in Rock Samples Under Mechanical Stress, *Water Re-
670 sources Research* 22 (4) (1986) 570–580. doi:10.1029/WR022i004p00570.
671 URL <http://doi.wiley.com/10.1029/WR022i004p00570>
- 672 [40] A. S. Grader, M. Balzarini, F. Radaelli, G. Capasso, A. Pellegrino,
673 Fracture-matrix flow: Quantification and visualization using X-Ray
674 computerized tomography, 2000, pp. 157–168. doi:10.1029/GM122p0157.
675 URL <http://www.agu.org/books/gm/v122/GM122p0157/GM122p0157.shtml>
- 676 [41] S. Akin, A. Kovscek, Computed Tomography in Petroleum Engineering
677 Research, *Applications of X-ray Computed Tomography in the Geosciences*
678 215 (2003) 23–38.
- 679 [42] A. Polak, D. Elsworth, H. Yasuhara, A. S. Grader, P. M. Halleck,
680 Permeability reduction of a natural fracture under net dissolution by
681 hydrothermal fluids, *Geophysical Research Letters* 30 (20) (2003) 1–4.
682 doi:10.1029/2003GL017575.
- 683 [43] B. R. Ellis, J. P. Fitts, G. S. Bromhal, D. L. McIntyre, R. Tappero, C. A.
684 Peters, Dissolution-driven permeability reduction of a fractured carbon-
685 ate caprock, *Environmental Engineering Science* 30 (4) (2013) 187–193.
686 doi:10.1089/ees.2012.0337.

- 687 [44] H. Deng, J. P. Fitts, D. Crandall, D. McIntyre, C. A. Peters, Al-
688 terations of Fractures in Carbonate Rocks by CO₂-Acidified Brines,
689 Environmental Science and Technology 49 (16) (2015) 10226–10234.
690 doi:10.1021/acs.est.5b01980.
- 691 [45] C. Zahasky, T. Kurotori, R. Pini, S. M. Benson, Positron emission to-
692 mography in water resources and subsurface energy resources engineer-
693 ing research, Advances in Water Resources 127 (March) (2019) 39–52.
694 doi:10.1016/j.advwatres.2019.03.003.
695 URL <https://doi.org/10.1016/j.advwatres.2019.03.003>
- 696 [46] C. Zahasky, D. Thomas, J. Matter, K. Maher, S. M. Benson, Multimodal
697 imaging and stochastic percolation simulation for improved quantification
698 of effective porosity and surface area in vesicular basalt, Advances in Water
699 Resources 121 (June) (2018) 235–244. doi:10.1016/j.advwatres.2018.08.009.
700 URL <https://doi.org/10.1016/j.advwatres.2018.08.009>
- 701 [47] S. Li, L. Liu, P. Chai, X. Li, J. He, Z. Zhang, Journal of Petroleum Sci-
702 ence and Engineering Imaging hydraulic fractures of shale cores using com-
703 bined positron emission tomography and computed tomography (PET-
704 CT) imaging technique, Journal of Petroleum Science and Engineering
705 182 (May) (2019) 106283. doi:10.1016/j.petrol.2019.106283.
706 URL <https://doi.org/10.1016/j.petrol.2019.106283>
- 707 [48] T. Kurotori, C. Zahasky, M. Gran, A. R. Kavscek, S. M. Ben-
708 son, Comparative analysis of imaging and measurements of micrometer-
709 scale fracture aperture fields within a heterogeneous rock using PET
710 and X-ray CT, Transport in Porous Media 147 (2023) 519–539.
711 doi:<https://doi.org/10.1007/s11242-023-01922-8>.
- 712 [49] C. Zahasky, S. M. Benson, Micro-Positron Emission Tomography for
713 Measuring Sub-core Scale Single and Multiphase Transport Parame-
714 ters in Porous Media, Advances in Water Resources 115 (2018) 1–16.

- 715 doi:10.1016/j.advwatres.2018.03.002.
716 URL <http://linkinghub.elsevier.com/retrieve/pii/S030917081731182X>
- 717 [50] C. R. Romano, C. Zahasky, C. Garing, J. M. Minto, S. M. Benson, Z. K.
718 Shipton, R. J. Lunn, Sub-core scale fluid flow behavior in a sandstone
719 with cataclastic deformation bands, *Water Resources Research* (2020) 1–
720 16doi:10.1029/2019wr026715.
- 721 [51] C. Zahasky, S. M. Benson, Preferential Solute Transport in Low Permeabil-
722 ity Zones During Spontaneous Imbibition in Heterogeneous Porous Media,
723 *Water Resources Research* 58 (1) (2022). doi:10.1029/2020wr029460.
- 724 [52] T. Kurotori, C. Zahasky, S. Hosseinzadeh Hejazi, S. Shah, S. Ben-
725 son, R. Pini, Measuring, imaging and modelling solute transport in
726 a microporous limestone, *Chemical Engineering Science* 196 (2019).
727 doi:10.1016/j.ces.2018.11.001.
- 728 [53] T. Kurotori, M. P. Murugesu, C. Zahasky, B. Vega, J. L. Druhan, S. M.
729 Benson, A. R. Kavscek, Mixed imbibition controls the advance of wetting
730 fluid in multiscale geological media, *Advances in Water Resources* 175
731 (2023) 104429. doi:<https://doi.org/10.1016/j.advwatres.2023.104429>.
732 URL <https://www.sciencedirect.com/science/article/pii/S0309170823000647>
- 733 [54] R. Pini, S. C. Krevor, S. M. Benson, Capillary pressure and het-
734 erogeneity for the CO₂/water system in sandstone rocks at reser-
735 voir conditions, *Advances in Water Resources* 38 (2012) 48–59.
736 doi:10.1016/j.advwatres.2011.12.007.
737 URL <http://linkinghub.elsevier.com/retrieve/pii/S0309170811002363>
- 738 [55] H. Aljamaan, C. M. Ross, A. R. Kavscek, Multiscale Imaging of Gas Storage
739 in Shales, *SPE Journal* 22 (06) (2017) 1760–1777. doi:10.2118/185054-PA.
740 URL <http://www.onepetro.org/doi/10.2118/185054-PA>
- 741 [56] A. F. Frangi, W. J. Niessen, K. L. Vincken, M. A. Viergever, Multiscale ves-
742 sel enhancement filtering, in: W. M. Wells, A. Colchester, S. Delp (Eds.),

- 743 Medical Image Computing and Computer-Assisted Intervention — MIC-
744 CAI'98, Springer Berlin Heidelberg, Berlin, Heidelberg, 1998, pp. 130–137.
- 745 [57] L. Li, L. Zhu, C. Ma, L. Lin, J. Yao, L. Wang, K. Maslov, R. Zhang,
746 W. Chen, J. Shi, L. V. Wang, Single-impulse panoramic photoacoustic
747 computed tomography of small-animal whole-body dynamics at high spa-
748 tiotemporal resolution, *Nature Biomedical Engineering* 1 (5) (2017) 0071.
749 doi:10.1038/s41551-017-0071.
750 URL <http://www.nature.com/articles/s41551-017-0071>
- 751 [58] Y. Liu, L. Peng, S. Huang, X. Wang, Y. Wang, Z. Peng,
752 River detection in high-resolution sar data using the frangi fil-
753 ter and shearlet features, *Remote Sensing Letters* 10 (10) (2019)
754 949–958. arXiv:<https://doi.org/10.1080/2150704X.2019.1635286>,
755 doi:10.1080/2150704X.2019.1635286.
756 URL <https://doi.org/10.1080/2150704X.2019.1635286>
- 757 [59] R. N. Horne, F. Rodriguez, Dispersion in tracer flow in fractured
758 geothermal systems, *Geophysical Research Letters* 10 (4) (1983) 289–292.
759 doi:10.1029/GL010i004p00289.
760 URL <http://doi.wiley.com/10.1029/GL010i004p00289>
- 761 [60] I. Ippolito, E. J. Hinch, G. Daccord, J. P. Hulin, Tracer dispersion in 2-D
762 fractures with flat and rough walls in a radial flow geometry, *Physics of*
763 *Fluids A* 5 (8) (1992) 1952–1962. doi:10.1063/1.858822.
- 764 [61] J. Bodin, F. Delay, G. de Marsily, Solute transport in a single fracture with
765 negligible matrix permeability: 1. Fundamental mechanisms, *Hydrogeology*
766 *Journal* 11 (4) (2003) 418–433. doi:10.1007/s10040-003-0268-2.
- 767 [62] L. J. KLINKENBERG, ANALOGY BETWEEN DIF-
768 FUSION AND ELECTRICAL CONDUCTIVITY IN
769 POROUS ROCKS, *GSA Bulletin* 62 (6) (1951) 559–564.

- 770 arXiv:[https://pubs.geoscienceworld.org/gsa/gsabulletin/article-](https://pubs.geoscienceworld.org/gsa/gsabulletin/article-pdf/62/6/559/3441164/i0016-7606-62-6-559.pdf)
771 [pdf/62/6/559/3441164/i0016-7606-62-6-559.pdf](https://pubs.geoscienceworld.org/gsa/gsabulletin/article-pdf/62/6/559/3441164/i0016-7606-62-6-559.pdf), doi:10.1130/0016-
772 7606(1951)62[559:ABDAEC]2.0.CO;2.
773 URL [https://doi.org/10.1130/0016-7606\(1951\)62\[559:ABDAEC\]2.0.CO;2](https://doi.org/10.1130/0016-7606(1951)62[559:ABDAEC]2.0.CO;2)
- 774 [63] J. van Brakel, P. Heertjes, Analysis of diffusion in macroporous media
775 in terms of a porosity, a tortuosity and a constrictivity factor, Inter-
776 national Journal of Heat and Mass Transfer 17 (9) (1974) 1093–1103.
777 doi:10.1016/0017-9310(74)90190-2.
- 778 [64] S. Li, Z. Li, Q. Dong, Diffusion coefficients of supercritical CO₂ in oil-
779 saturated cores under low permeability reservoir conditions, Journal of CO₂
780 Utilization 14 (2016) 47–60. doi:10.1016/j.jcou.2016.02.002.
781 URL <http://dx.doi.org/10.1016/j.jcou.2016.02.002>
- 782 [65] R. R. Ratnakar, B. Dindoruk, The Role of Diffusivity in Oil and Gas Indus-
783 tries: Fundamentals, Measurement, and Correlative Techniques, Processes
784 10 (6) (2022) 1194. doi:10.3390/pr10061194.
785 URL <https://www.mdpi.com/2227-9717/10/6/1194>
- 786 [66] N. A. Mumallah, Hydrochloric acid diffusion coefficients at acid-fracturing
787 conditions, Journal of Petroleum Science and Engineering 15 (2) (1996)
788 361–374. doi:[https://doi.org/10.1016/0920-4105\(95\)00086-0](https://doi.org/10.1016/0920-4105(95)00086-0).
789 URL <https://www.sciencedirect.com/science/article/pii/0920410595000860>
- 790 [67] Q. Zhou, H. H. Liu, F. J. Molz, Y. Zhang, G. S. Bodvarsson, Field-scale
791 effective matrix diffusion coefficient for fractured rock: Results from liter-
792 ature survey, Journal of Contaminant Hydrology 93 (1-4) (2007) 161–187.
793 doi:10.1016/j.jconhyd.2007.02.002.
- 794 [68] L. W. Gelhar, C. Welty, K. R. Rehfeldt, A Critical Review of Data on
795 Field-Scale Dispersin in Aquifers, Water Resources Research 28 (7) (1992)
796 1955–1974. arXiv:arXiv:1011.1669v3, doi:10.1029/92WR00607.

- 797 [69] B. Krooss, R. Schaefer, Experimental measurements of the diffusion
798 parameters of light hydrocarbons in water-saturated sedimentary rocks—I.
799 A new experimental procedure, *Organic Geochemistry* 11 (3) (1987)
800 193–199. doi:10.1016/0146-6380(87)90022-2.
801 URL <https://linkinghub.elsevier.com/retrieve/pii/0146638087900222>
- 802 [70] V. Rebour, J. Billiotte, M. Deveughele, A. Jambon, C. L. Guen, Molecu-
803 lar diffusion in water-saturated rocks: A new experimental method, *Jour-
804 nal of Contaminant Hydrology* 28 (1-2) (1997) 71–93. doi:10.1016/S0169-
805 7722(96)00051-4.
- 806 [71] M. G. Rezk, J. Foroozesh, A. Abdulrahman, J. Gholinezhad, CO₂Diffusion
807 and Dispersion in Porous Media: Review of Advances in Experimental
808 Measurements and Mathematical Models, *Energy and Fuels* 36 (1) (2022)
809 133–155. doi:10.1021/acs.energyfuels.1c03552.
- 810 [72] S. Li, Y. Wang, K. Zhang, C. Qiao, Diffusion Behavior of Supercritical CO₂
811 in Micro- To Nanoconfined Pores, *Industrial and Engineering Chemistry
812 Research* 58 (47) (2019) 21772–21784. doi:10.1021/acs.iecr.9b04750.
- 813 [73] B. M. Krooss, D. Leythaeuser, Experimental measurements of the diffusion
814 parameters of light hydrocarbons in water-saturated sedimentary rocks-II.
815 Results and geochemical significance, *Organic Geochemistry* 12 (2) (1988)
816 91–108. doi:10.1016/0146-6380(88)90247-1.
- 817 [74] C. Noiriel, B. Madé, P. Gouze, Impact of coating develop-
818 ment on the hydraulic and transport properties in argillaceous
819 limestone fracture, *Water Resources Research* 43 (9) (2007).
820 arXiv:<https://agupubs.onlinelibrary.wiley.com/doi/pdf/10.1029/2006WR005379>,
821 doi:<https://doi.org/10.1029/2006WR005379>.
822 URL <https://agupubs.onlinelibrary.wiley.com/doi/abs/10.1029/2006WR005379>
- 823 [75] J. Du, L. Hu, J. N. Meegoda, G. Zhang, Shale softening: Observations,
824 phenomenological behavior, and mechanisms, *Applied Clay Science* 161

- 825 (2018) 290–300. doi:<https://doi.org/10.1016/j.clay.2018.04.033>.
826 URL <https://www.sciencedirect.com/science/article/pii/S0169131718301935>
- 827 [76] C. Zahasky, M. Murugesu, T. Kurotori, C. Sutton, J. Druhan, B. Vega,
828 S. M. Benson, A. Kavscek, Solute transport maps in a naturally fractured
829 shale rock before and after acidified brine injection - 4D imaging dataset
830 and analytical model (2023). doi:<https://doi.org/10.25740/pv902jr5822>.
- 831 [77] C. I. Steefel, S. Molins, Crunchflow, Software for modeling multicomponent
832 reactive flow and transport. User’s manual. Lawrence Berkeley National
833 Laboratory, Berkeley (2009).
- 834 [78] Q. Li, A. D. Jew, G. E. Brown Jr, J. R. Bargar, K. Maher, Reactive
835 transport modeling of shale–fluid interactions after imbibition of fracturing
836 fluids, *Energy & Fuels* 34 (5) (2020) 5511–5523.
- 837 [79] H. C. Helgeson, W. M. Murphy, P. Aagaard, Thermodynamic and kinetic
838 constraints on reaction rates among minerals and aqueous solutions. ii. rate
839 constants, effective surface area, and the hydrolysis of feldspar, *Geochimica
840 et Cosmochimica Acta* 48 (12) (1984) 2405–2432.
- 841 [80] J. L. Palandri, Y. K. Kharaka, A compilation of rate parameters of water-
842 mineral interaction kinetics for application to geochemical modeling, Tech.
843 rep., Geological Survey Menlo Park CA, Menlo Park, CA (United States)
844 (2004).
- 845 [81] L. Chou, R. Wollast, Steady-state kinetics and dissolution mechanisms of
846 albite, *American Journal of Science* 285 (10) (1985) 963–993.
- 847 [82] M. A. McKibben, H. L. Barnes, Oxidation of pyrite in low tempera-
848 ture acidic solutions: Rate laws and surface textures, *Geochimica et Cos-
849 mochimica Acta* 50 (7) (1986) 1509–1520.
- 850 [83] A. Bauer, G. Berger, Kaolinite and smectite dissolution rate in high molar
851 koh solutions at 35 and 80 c 13 (7) (1998) 905–916.

852 [84] M. Alkattan, E. H. Oelkers, J.-L. Dandurand, J. Schott, Experimental
853 studies of halite dissolution kinetics, 1 the effect of saturation state and the
854 presence of trace metals, *Chemical Geology* 137 (3-4) (1997) 201–219.